Resonating AlN-thin film MEMS mirror with digital control

Konsta Ruotsalainen,* **Dmitry Morits, Oili M. E. Ylivaara, and Jukka Kyynäräinen**
VTT Research Centre of Finland Ltd., Espoo, Finland

Abstract. Piezoelectrically actuated resonant micromirrors were designed to meet the light detection and ranging (LiDAR) system requirements. Key features were a 3-mm mirror aperture, a 40-deg field of view, and a 50-Hz refresh rate. The presented micromirror provides biaxial symmetrical beam steering with ± 12.7 deg mechanical tilt angle, resulting in a 50-deg field of view with an adjustable Lissajous XY-scanning pattern for a forward-looking LiDAR system. The mirrors were fabricated using silicon on insulator wafers, and actuation was based on piezoelectric aluminium nitride thin film. The mirrors were vacuum packaged for high-quality factor resonator operation. The device design contained eight separate piezoelectric aluminium nitride elements arranged as differential pairs for each axis, where each actuator was equipped with a sensing element providing a mechanically coupled electrical feedback signal. The piezoelectric elements connected as actuators required only minimal power and were directly compatible with CMOS low-voltage logic, which eases integration to driving digital systems. The sense elements are used to monitor phase, amplitude, and frequency. A digital control system connected to each of these elements provides accurate frequency and phase control of independent orthogonal resonators, permitting control of the X and Y amplitudes and the refresh rate of the Lissajous pattern. [DOI: 10.1117/1.JOM.2.1.011006]

Keywords: piezoelectric effect; mirrors; scanning; microelectromechanical systems; electronics; logic.

Paper 21023SS received Oct. 8, 2021; accepted for publication Jan. 27, 2022; published online Feb. 16, 2022.

1 Introduction

Advanced driver-assistance systems and, more generally, autonomous vehicles of any size or type are and will be using light detection and ranging (LiDAR) systems for mapping their surroundings and providing data for decision making. Microelectromechanical system (MEMS)-based scanning elements aim to solve the need for miniaturization and cost reduction of LiDAR systems while maintaining high performance in key parameters such as range, angular resolution, and scan rate. Various methods have been applied to miniaturize the optical scanning elements of the LiDAR system, such as the two-mirror systems presented by Wang et al.[1] and Nguyen et al.[2] or the wobbling mirror for circular scanning presented by Pensala et al.[3] and Hoffman et al.[4] This work is concentrated on a single-mirror approach for a 2D-scanning pattern suitable for use in forward-looking LiDARs. Different types of 2D-scanning LiDARs have been reported based on PZT-elements[5] and electrothermal,[6,7] electromagnetic,[8] or electrostatic actuators.[9] Actuators fabricated on the aluminium nitride (AlN) thin-film-based process offer comparable performance levels with other state-of-the-art 2D scanning techniques, in which the tilt angle and the mirror size are mainly limited by mechanical considerations. The main benefit of vacuum packaged AlN-based actuators is the possibility of using CMOS compatible drive levels, allowing for direct control of mirror resonators with digital integrated circuits. AlN is compatible with the CMOS processing technology, and due to its reasonable piezoelectric coefficient of 5.15 pm/V for d_{33} and low permittivity of 10.7, it is a suitable material for micromirror actuation and sensing.[10] The evolution of devices and processes presented by Pensala et al.[3] is

*Address all correspondence to Konsta Ruotsalainen, konsta.ruotsalainen@vtt.fi

tailored for a 2D-beam steering automotive forward-looking MEMS LiDAR. As the LiDAR is a highly optimized and performance-driven system, the optimization of each key component is essential. In this paper, an MEMS mirror is designed, fabricated, and characterized with a fully digital FPGA-based control method. The MEMS mirror design section covers the mirror design process with LiDAR system parameters affecting the design. The microfabrication of the mirror is described in Sec. 3. Section 4 includes the digital electronics design and the characterization of the system. Section 5 contains a discussion and comparison with other work, and finally, conclusions are presented in Sec. 6.

2 MEMS Mirror Design

MEMS mirror specifications were defined to meet the requirements of the LiDAR system while taking into account the limitations and capabilities of the fabrication process. The intended target application for the mirror is a coaxial forward-looking LiDAR, in which both outbound and inbound optical signals are reflected by the mirror. For a coaxial transceiver, mirror rotation between outbound and inbound events should be minimized. Ideally, the mirror should move only between measurement points. A compromise between the scanning area and speed is required. Suitable values for a forward-looking LiDAR were selected: a ± 10-deg mechanical tilt angle and a 1 kHz resonance frequency with a 10% difference between orthogonal axes. These selections provide a rectangular scan area in front of the vehicle with a refresh rate of about 50 Hz. This scanning method is rarely used in LiDAR systems compared with the more common raster scanning,[5,7,8] in which one axis is fast and the other axis is slow. When both axes are driven with only a small frequency difference between them, the resulting almost uniform XY-movement enables measurements evenly around the scan area. Based on simulations of mirror angular speed, dynamic deformation, and optical needs, the mirror diameter was selected to be 3 mm. The simulated dynamic deformation is 320 nm peak-to-peak. In general, dynamic deformation reduces the performance of the LiDAR as beam divergence is affected by the scanning element. After the mechanical tilt angle, resonance frequency, and mirror diameter are selected, the design can be optimized within the limitations of a manufacturing process. The combination of design parameters and the piezoelectric AlN-thin film MEMS platform requires the use of high-quality factor resonators. Suitable resonators are attainable with vacuum packaging in the range of 0.1 to 1 Pa, allowing large mechanical tilt angles to be reached with low drive voltages. The AlN sense elements, mechanically coupled to the actuators, provide a real-time mirror position signal. The position signal is captured by the controller presented in Sec. 4.1, allowing for synchronization between the LiDAR system and the mirror movement. The full set of mirror specifications is shown in Table 1.

Table 1 Specifications of MEMS scanning mirrors.

Parameter	Specification
Chip dimension	$7 \times 7 \times 2.5$ mm
Movable structure	Single-crystal silicon, thickness 50 μm
Control and sensing	1.5 μm piezoelectric aluminium nitride thin film
Packaging	Wafer-level packaging with controlled low pressure
Optical aperture	3 mm (diameter)
Scanning type	Resonant XY, independent
Max tilt angle	± 10 deg
Resonant frequency	1000 Hz
Refresh rate	50 Hz
Position sensing	AlN elements within main actuator beams

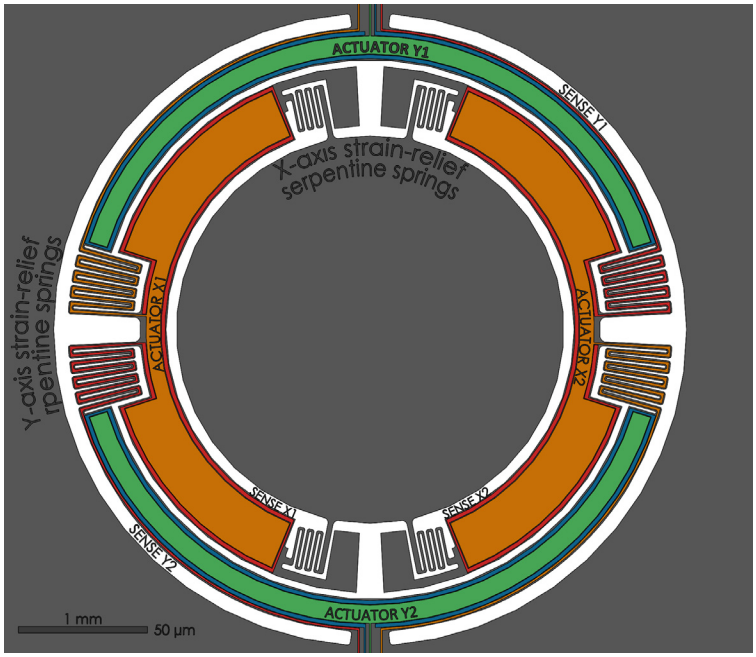

Fig. 1 The strain-relief springs; blue *Y*-sense elements around green *Y*-actuators and red *X*-sense elements wrapping around orange *X*-actuators.

The mirror has two orthogonal sets of concentric differential actuators applying torsion to the mirror plate. The mirror deflection is amplified by attaching the actuators close to the rotation axes. The sensing AlN elements are located concentrically around larger AlN-actuator elements on the same actuator beams. The concentric design elements are coupled to each other by strain-relief serpentine springs. The strain-relief serpentine springs reduce the twisting stress between the actuators and the mirror, allowing balanced actuator beams to bend without an in-plane movement of the connection points. The discrete AlN elements are contained within concentric actuator beams, and the top and bottom metallization enveloping the AlN continues to the contact pads. The structure of the MEMS mirror is presented and annotated in Fig. 1.

Modeling and optimization of the micromirror geometry was done by numerical simulations using COMSOL Multiphysics software without geometric nonlinearity built into the models. The optimization of the piezoelectric actuators was crucial not only to reaching large tilt angles but also to providing robustness against mechanical breakage. The simulated stress levels at maximum tilt angle were kept below 1 GPa to provide safety buffers against external stimuli, such as vibration and shock coming from the environment. The vacuum cavity height was

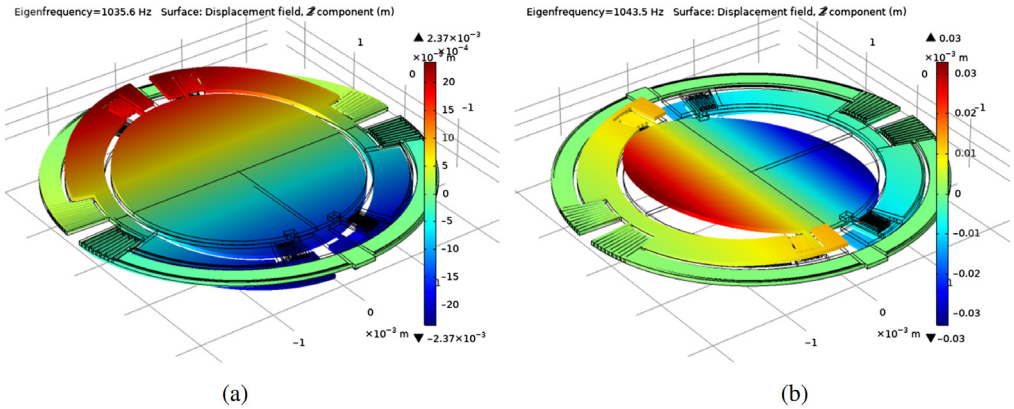

Fig. 2 A COMSOL model of mirror displacement in single-axis excitation modes. (a) *Y* axis and (b) *X* axis resonance simulations.

limited by the wafer thickness to 650 μm, limiting the maximum movement range to ± 25.7 deg for the X axis and to ± 18.6 deg for the Y axis. Simulated deflections of the mirror with a ± 10 deg tilt angle for the X and Y axes movements are presented in Fig. 2, leaving a height margin of 300 μm between the mirror plate and cavity walls.

3 Microfabrication

The micromirror elements were fabricated at a VTT Micronova cleanroom, and the wafers were vacuum packaged at Murata Electronics Oy. Micromirror fabrication was based on SOI-wafer technology, in which the device layer defined the thickness of the mirror elements. The key parameters of the SOI-wafers are summarized in Table 2.

Unlike most of the SOI-wafers used in MEMS applications, the device layer had (111) orientation to reduce or eliminate the effect of crystal orientation to the mechanical spring constant. The fabrication of the resonating elements was based on VTT's piezoMEMS platform.[3] A thick, 1500-nm piezoelectric AlN actuator was sputtered on a molybdenum bottom electrode. Piezoelements were patterned with TMAH wet etching and were covered with oxide made by plasma enhanced chemical vapor deposition. Oxide was further patterned to make contact holes for the top electrode; sputtered molybdenum was used as the top electrode material. After top electrode patterning, mirror elements were defined by photolithography and etched to the silicon device using deep reactive ion etch (DRIE), etching was stopped at buried oxide. Mirror elements were released by etching a 650-μm deep cavity into the handle wafer with DRIE. Finally, the mirror area was coated with an evaporated reflective metal layer. The wafers with micromirrors were vacuum packaged using glass and silicon wafers capping on the front and back sides, respectively. The actuator side contained the electrical interconnects, and the mirror capping was a simple glass wafer to allow the laser light to reach the metal coated mirror. To accommodate the large deflection of the mirror element, correspondingly large recesses were etched in cap wafer. Figure 3 shows an overall cross section of the MEMS micromirror, including the piezoelectric AlN elements on the top side and sputtered gold on the bottom side of the mirror plate with the packaging.

Murata Electronics Oy processed the final device packaging, including the cap wafer processing, anodic bonding of the wafers, and mounting of the finalized components to ceramic carriers. The anodic bonding was done in a single step, in which mirror wafers, silicon cap wafers, and glass wafers were brought into contact simultaneously at an elevated temperature, and high voltage was applied. The drawback of this packaging method is that it does not allow for the deposition of an antireflective coating on the glass cap wafer because it would not survive the high-temperature bonding. The fabrication process was finalized by dicing and by attachment of ceramic carrier boards presented in Fig. 4, enabling easy mirror changes in the test setup.

Table 2 SOI-wafer parameters.

Parameter	Value
Wafer type	SOI
Diameter	150 ± 0.2 mm
Device layer thickness	52 ± 2.0 μm
Buried oxide thickness	1000 ± 50 nm
Handle wafer thickness	650 ± 5 μm
Conductivity type	P+
Crystal orientation	[111] ± 0.5 deg
Resistivity range	0.007 to 0.020 Ohm-cm

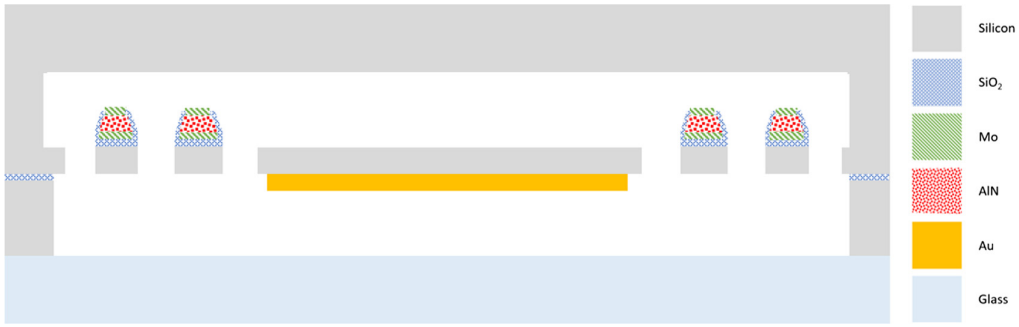

Fig. 3 Simplified MEMS mirror cross section with AlN-elements and gold mirror.

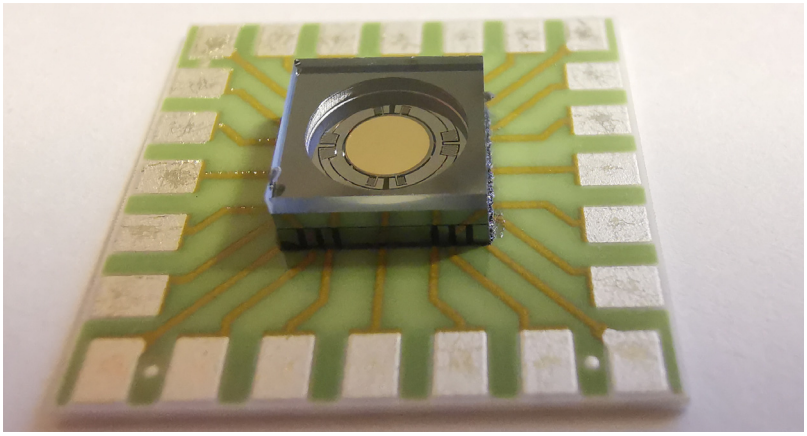

Fig. 4 Biaxial MEMS mirror on ceramic breakout board.

4 Results

The maximum mechanical tilt angles were measured by sweeping the excitation frequency upward through the resonance. Figure 5 shows an example of the dependence of the mechanical tilt angle on the driving frequency when a single-resonance axis is actuated at a time.

In Fig. 5, the curvature of the angle versus frequency curves present a typical Duffing effect. The Duffing nonlinearity is a well-known phenomenon in silicon resonators:[11,12] the stress-induced stiffening of the silicon beam bends the resonance curve and therefore lessens the amplitude to frequency ratio compared with a nonstiffening resonator. This effect is highly useful in Lissajous-mode scanning as a low amplitude to frequency ratio enables the selection of frequencies for each axis more freely without affecting the resonance amplitude.

4.1 *Electronics*

In the previous work,[13] a fully digital phase-locked loop (PLL) controller for micromirrors was presented. The evolution of that system is used for these mirrors to drive and maintain precise drive frequencies for differential actuators. The analog front end for this system is presented in Fig. 6, containing a three-state half-bridge buffer for simplified drive and a summing amplifier with a comparator as an analog to digital stage.

The analog front end presented in Fig. 6 captures the high-impedance signals with opposite polarities from the piezoelectric differential sense elements. Capturing sense signals with opposite polarities causes the rotation signals to be added together, whereas common-mode mechanical signals due to shocks or vibration are cancelled out, improving the signal-to-noise ratio. On the drive side, benefits of a three-state drive are twofold. From an experimental perspective,

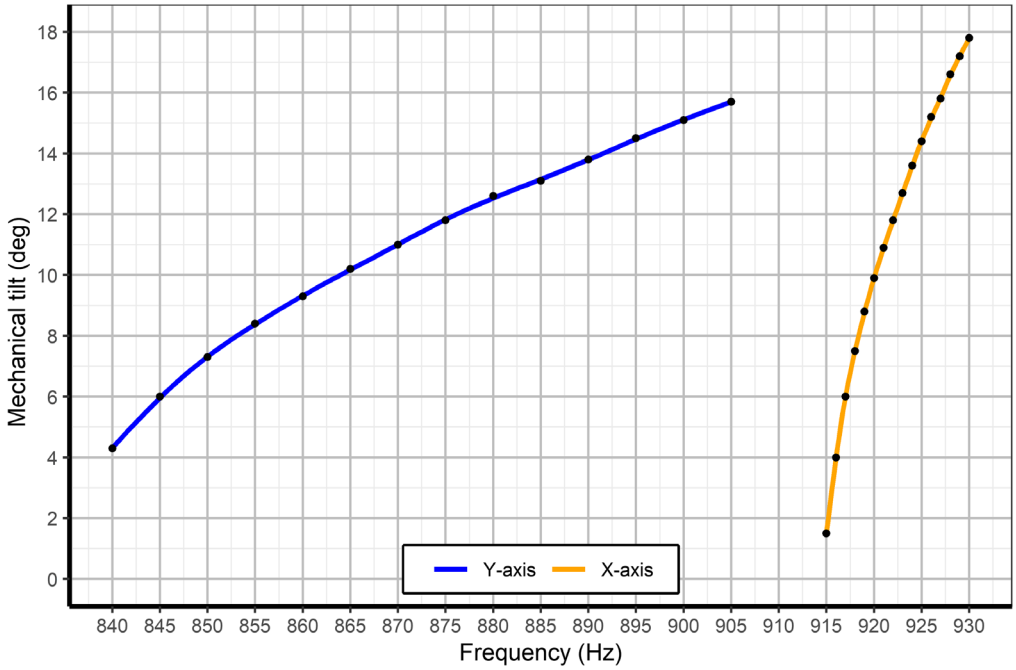

Fig. 5 Measured angle versus frequency curves of independent axis of the MEMS mirror.

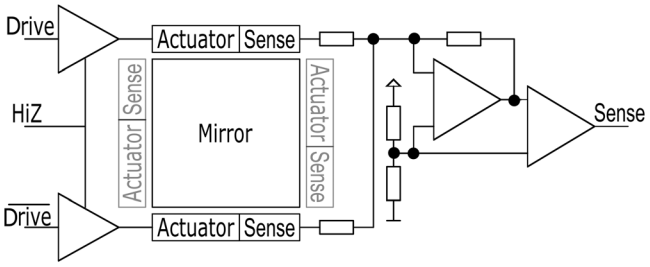

Fig. 6 Analog front end for the MEMS mirror.

the benefits of a three-state drive are separation of digital and analog domains and the ability to test different drive voltages. From system architecture perspective, the three-state drive allows for an accurate power adjustment via pulse-width modulation techniques and an ability to set the MEMS elements to a high-impedance state. The mirror drive systems, sensing amplifiers, and comparators were supplied from a single 3.3-V supply.

The digital mirror controller design is implemented with Verilog hardware description language. This digital design utilizes 879 logic cells and 567 registers when loaded into a MAX10 FPGA by Intel. The controller architecture allows for fast adaptation to different element configurations as drive and sense pairs can be separated or combined depending on the topology of the MEMS device. The implementation of the controller by a programmable logic allows for multiple feedback routes and control methods without compromising the low-latency synchronized operation of the controller. The digital design integrates the required frequency generator start-up circuitry, reset, and state machines. The design block diagram for two independent resonators is presented in Fig. 7.

The presented system allows for a selection between open- and closed-loop operations. The Lissajous patterns presented in Secs. 4.2 and 4.4 are all taken with the open-loop test mode, in which parametric frequency sweep excites the resonators to predetermined resonances. An FPGA-system driven square wave has a basic period resolution of 8 ns derived from a 125-MHz system clock. With resonance frequencies at 915 Hz, a single 8-ns step changes the frequency by 7 mHz. To increase the frequency resolution, a 46-bit phase accumulator was included in the

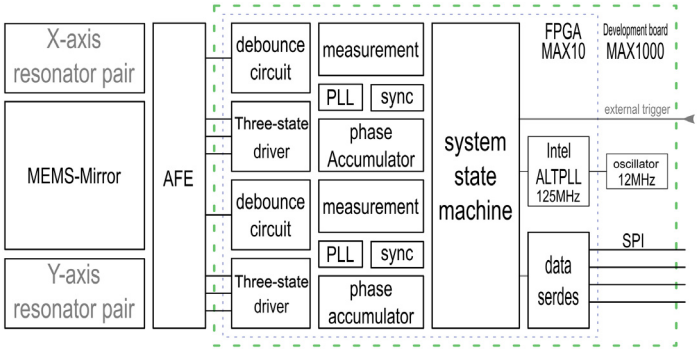

Fig. 7 Digital resonance controller design for XY-mirrors.

design. The phase accumulator allows for a very flexible parametric frequency sweep and high-resolution frequency output. The expression $\frac{1}{2^N * \mathrm{CLK}}$ describes the phase accumulator resolution dependency on the number of bits in the accumulator (N) and on the frequency of the FPGA system clock (CLK). With 46 bits used for a phase accumulator, the resolution is 1.78 μHz independent of the frequency selection. The system offers two solutions to record the position of the micromirror. The primary method is based on phase signal derived from the AlN sense elements and measured with a counter running at a 125 MHz system clock. This method gives accurate real-time timing information that is captured at the rising or falling edges of a trigger event coming from internal or external sources. The precision of this method is limited by the system clock period of 8 ns, which with a 915 Hz resonant frequency yields 46-μrad angular resolution. The secondary method for capturing the mirror position is by directly recording the drive side phase accumulator value, i.e., the high-resolution presentation of the phase. The drive side capture of phase information offers more precision, whereas the accuracy of phase information is not as good as there is a varying phase difference between the drive signal and the mirror movement. The phase difference varies depending on the operation point of the oscillation, which is affected by many factors, such as the three-state duty cycle, temperature, frequency, and element properties. The hybrid of these modes is used when Lissajous pattern synchronization is engaged; in this hybrid mode, phase accumulator phases of one resonator are captured with the rising edge of the sense signal of another resonator. When the ratio of the X and Y scanning frequencies is rational, the phase difference at the rising edge of the sense signal has a repeating pattern. By capturing the minimum of the repeating phase difference pattern, a reference point for a static Lissajous pattern is established. By changing one of the frequencies slightly, we can induce a slowly changing pattern, in which the phase difference minimum changes over time. When the minimum reaches the desired value, the pattern change is halted by reverting the frequencies to an exact frequency ratio.

4.2 *Q-Factor*

The quality factor of the micromirror was recorded using a damping method in which the oscillation drive is cut off and the decaying oscillation curve is measured. The X axis resonator was driven to resonance at 915 Hz in the open-loop configuration, and an amplitude of 509 mV was measured with a Tektronix MSO460 oscilloscope. The cutoff event disconnects the mirror driver power supply, and decaying oscillations are measured with the oscilloscope. Measuring the time between the last drive signal and the $1/e$-point at the attenuation curve yields a result of 6.24 to 6.26 s. The Q-factor calculation is presented in the following equation:

$$Q = \frac{\tau \omega_N}{2} = \pi * 915\ \mathrm{Hz} * 6.25\ \mathrm{s} \approx 18{,}000. \tag{1}$$

4.3 *Optical Test Setup*

For the system level optical characterization, the optical setup utilizes a 635-nm diode laser and a mechanical support for the micromirror. The laser beam reflected by the mirror is projected on a

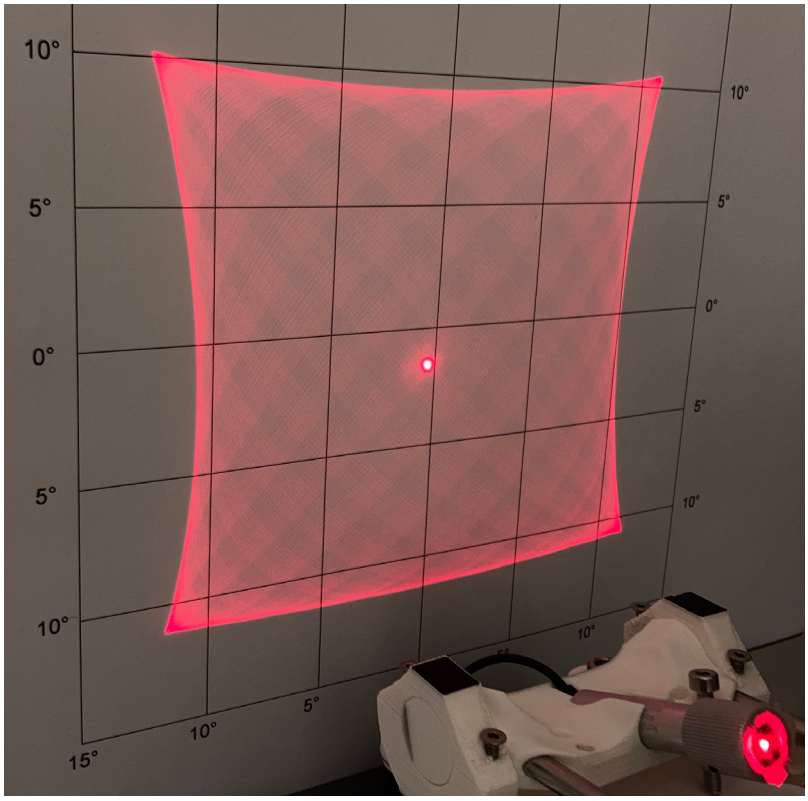

Fig. 8 The projector setup; the screen axes were calibrated to correspond to mechanical tilt angles utilizing a small power laser targeted to the mirror.

calibrated optical target, allowing for measurements of the mirror tilt angle by visual observation of the laser beam pattern. In the center of the pattern, one can see a bright spot due to the reflection from the plain glass cap wafer. In Ref. 14, the glass reflection is solved by aligning the reflection out of the scanning pattern. The projector type of test setup allows for straightforward distance measurements of the projected pattern, with measurement accuracy limited mostly by the fuzzy edge of the laser beam. Uncertainty of the measurement point is mostly dominant at small dimensions, and therefore results under 4 deg are not presented here. Another error source arises from various optical distortions of the pattern, making repeatable measurements difficult. In this case, the shortest dimensions between the pattern edges were used to define the angle. On the corners where the pincushion effect distorts the pattern, angles are somewhat larger.

The shape nonuniformity of the Lissajous patterns in Figs. 8 and 9, in which the bottom edge has a barrel distortion instead of the pincushion distortion on the other edges, is due to a nonsymmetric projection as the laser source is at a 20-deg angle from the mirror normal. The varying incident angle between the laser scanning pattern and the planar glass wafer causes the varying angle of refraction on air–glass boundaries. Corrections for these distortions could be designed into the optics or distortion correction algorithms[15–17] may be used to compensate for the distortions in an imaging application. Figure 8 presents a varying scanning pattern that meets the design specifications.

4.4 *Lissajous Patterns*

In Fig. 8, the *X* and *Y* axes' frequencies for the pattern are 861.018 and 915.074 Hz, respectively. The frequencies were derived from the system clock cycles driving the circuit. The selection of frequencies in Fig. 8 is optimized for a rapidly changing pattern; the frequency ratio between the *X* axis and the *Y* axis determines how much the scanning pattern changes during each cycle. The change of the phases leads to a high fill ratio of the scanning pattern as all possible combinations

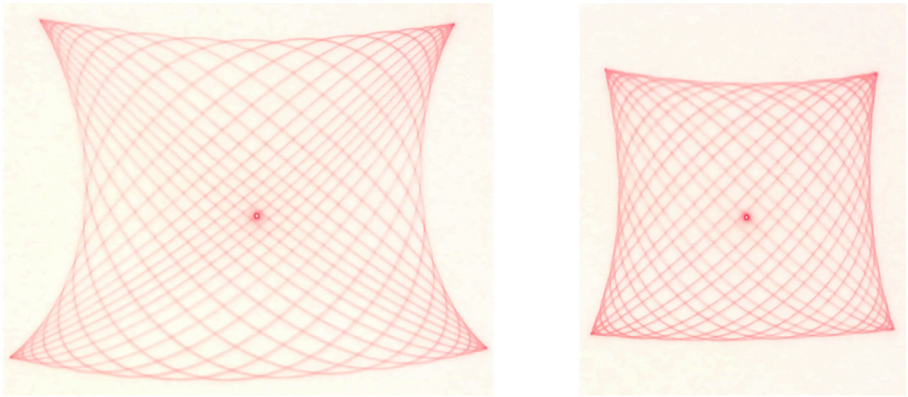

(a) X:12.8° Y:12.7° Lissajous pattern (b) X:10.6° Y:10.4° Lissajous pattern

Fig. 9 Frequency and phase matched Lissajous patterns: (a) *X*: 12.8 deg, *Y*: 12.7 deg and (b) *X*: 10.6 deg, *Y*: 10.4 deg.

of phases between the frequencies are invoked. The change of the phases leads to a high fill ratio of the scanning pattern as all possible combinations of phases between the frequencies are invoked. The image presented in Fig. 8 was taken with a 1/20 s shutter speed so that the change in pattern was captured over multiple cycles. The images combined in Fig. 9 were captured with the same imaging settings, but with different drive parameters. In Fig. 9(a), the maximum mechanical tilt angles were about 12.8 deg on the *X* axis and 12.7 deg on the *Y* axis, limited by the diagonal tilt angle close to the design maximum. In Fig. 9(b), the tilt angles are limited to the specified ± 10 deg, and the pattern has much less distortion as the diagonal angles are also smaller.

In Fig. 9(a), a scanning pattern is established with a 34/35 frequency ratio, with the *X* axis resonance at 915.053766 Hz and the *Y* axis at 888.909373 Hz. The phase accumulator synchronization, introduced in Sec. 4.1, was enabled to match the scanning lines on top of each other, effectively doubling the refresh rate of the pattern to 52.3 Hz. As the design specifications for the pattern were ± 10 deg for a rectangular area, the frequencies were adjusted to 915.042175 Hz for the *X* axis and 861.216165 Hz for the *Y* axis, providing a frequency ratio of 16/17 and a pattern refresh rate of 53.8 Hz. The phase difference for the pattern in the image is tuned to space the scanning lines equally inside the pattern to provide an equal distribution of possible 3D-point vector measurement locations.

The simple rational ratio between the Lissajous frequencies eases the generation of the measurement algorithm as the same coordinates can be measured again at 50 Hz intervals. Measuring the same coordinates requires careful planning of frequencies and the open-loop operation mode to stabilize the oscillation to the desired frequency. In the phase-locked closed-loop operation mode, the exact frequency could not be forced, therefore leaving the closed-loop system more suited for scanning patterns not requiring an exact control of the frequency or the pattern.

4.5 *Cross-Axis Coupling*

The cross-axis amplitude measurement result in Fig. 10 explains the difference between Lissajous-pattern frequencies and frequencies presented in Fig. 5.

In Fig. 10, cross-talk coupling causes a shift of the frequency that is proportional to the amplitude of the orthogonal axis. The resonance amplitude of the *X* axis is 4.7 deg, which corresponds to *X* axis data in Fig. 5, with the *Y* axis at rest. When the resonance amplitude on the *Y* axis increases, the stress and therefore the spring constant change on the orthogonal axis also, which in turn results in an operation point with a higher amplitude. The amount of this frequency shift could be adjusted by changing the strain-relief serpentine spring structures presented in Fig. 1.

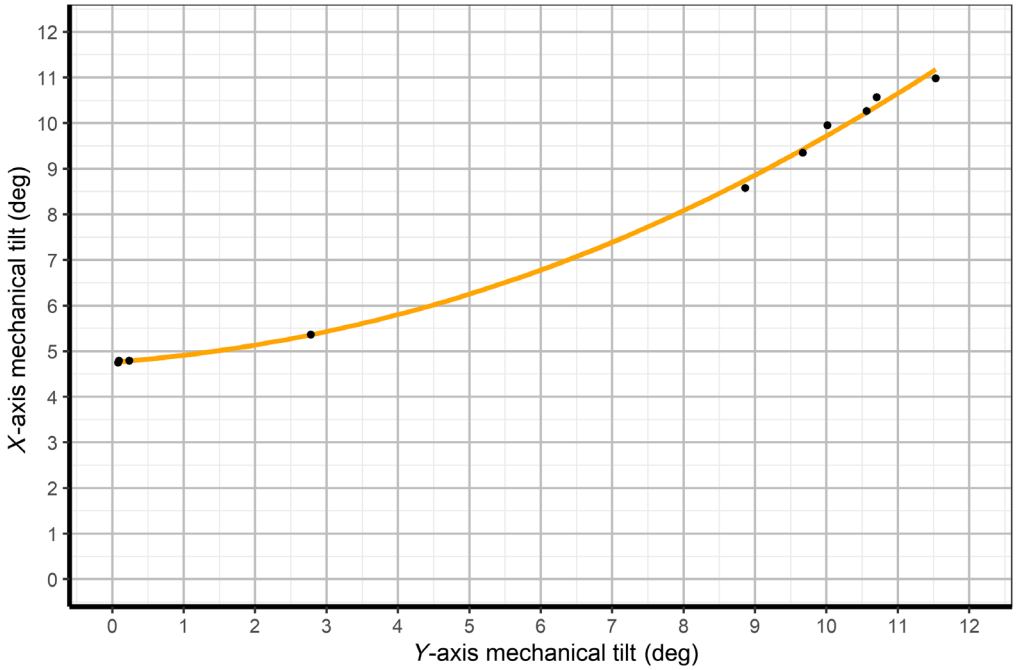

Fig. 10 The *X* axis resonance amplitude at 915 Hz versus the *Y* axis resonance amplitude.

5 Discussion

During micromirror characterization, it was observed that to reach large and stable tilt angles, resonant MEMS micromirrors must operate in a nonlinear regime. This nonlinearity was observed already by Pensala et al.,[3] and it is due to stress-induced stiffening of the actuator springs. In this regime, the dependence of the tilt angle on the frequency is described by a Duffing curve,[11] instead of a Lorenz resonance curve, typical for linear systems. Also cross-axis coupling was observed between the frequencies and amplitudes of the *X* and *Y* axes, complicating the prediction of the available scanning pattern from the linear simulations. Even though the pattern prediction was found to be challenging, the pattern generation was not as the Duffing effect in our case leads to an almost linear correlation between the frequency and the amplitude. The results presented here are well in line with other state-of-the-art micromirrors presented in Table 3.

The mirror behavior agrees well with the established theory of spring stiffening and simulated operation mode. The performance of the piezoelectric system compares well against other mirrors with various manufacturing technologies presented in Table 3, and the desired mode of operation is very good for coaxial LiDARs. Future research on micromirrors control should

Table 3 Comparison with other work.

Author	Actuators	Size	Frequency	Angle	Drive
Ben-Mrad and Pasiliao[9]	Electrostatic	ϕ1 mm	24 frames	±2.5 deg	200 V
Sarkar et al.[7]	Electrothermal	1.4 mm × 1.2 mm	5 kHz, 30 Hz	±16.25 deg, ±6.25 deg	3.3 V
Wang et al.[6]	Electrothermal	1.4 mm × 1.2 mm	1.69 kHz	±3.5 deg	5 V
Yalcinkaya et al.[8]	Electromagnetic	ϕ1.5 mm	21 kHz, 4 kHz	±14.5 deg, ±16.25 deg	150 mA
Piot et al.[5]	PZT piezoelectric	ϕ1.5 mm	450 Hz, 25 kHz	±3.875 deg, ±1.5 deg	2 V, 5 V
This work	AlN piezoelectric	ϕ3 mm	915 Hz, 860 Hz	±12.8 deg, ±12.7 deg	3.3 V

address shortcomings of the presented system and advance the technology readiness level by introducing application environmental testing. One of the shortcomings of the mirror drive was a requirement for a predetermined operation point coming from an open-loop style of the start-up circuit. The start-up frequency sweep needs to be slow enough to maintain the correct phase between excited resonance and the drive signal. Another way to excite resonators would be a broad-spectrum start-up pulse with PLL locking into resonances awakened in the resonator. Although a PLL was determined to be unsuitable for precision pattern forming, it might still be a better way for the start-up, error handling, and backup operations. The weakness of a non-PLL approach for a resonator controls its inability to respond to shock events, pushing the excitation signal out of sync with movement. These shock-induced fail states require additional recovery mode development so that the system state machine responds and adjusts accordingly. More application development and safety assessments would be required to study required safety margins and recovery time requirements for automotive use of MEMS mirrors. A matter to consider is unwanted vibrations existing in any machine with moving parts, and undesired secondary vibration modes also exist in MEMS mirrors. Digital control logic with a non-PLL type of wake-up and control solves most of these as undesired frequency vibrations are not amplified, and fast controlled transitions over unwanted frequencies can move resonances to ranges not achievable with the PLL approach. The final application grade mirror controller would need to incorporate multiple feedback loops to provide a solution to different scenarios.

Another point of study would be the safety margin in real-life operation conditions with random vibrations and shocks. Although the micromirror with AlN-resonators can operate with 1.8 V voltage or lower, the higher voltages enable higher resonance amplitudes up to mechanical limits of the mirror design. Also empirical experience shows that the increase of operating voltage increases the robustness of the system as a larger disturbance is needed to desynchronize the sinusoidal movement of the mirror with the drive signal.

In light of the presented data, the AlN-based micromirror system would meet requirements for a good scanning element: the maximum mechanical tilt angles are up to ± 12.8 deg, the tilt angles can be adjusted digitally, the Lissajous-pattern frequency ratio can be selected and phases synchronized, and the real-time position information is available. However, the lack of experimental data on the mirror system behavior on shock and vibration scenarios leave the suitability for vehicle use to be studied.

6 Conclusion

A resonating piezoelectric micromirror was successfully designed, manufactured, and verified to meet given LiDAR application specifications. Near square output with a ± 10.4- deg mechanical tilt angle was achieved, and the design margins allowed for pushing the Lissajous pattern up to a ± 12.7 deg square with some distortion on the edges of the pattern. This showcases the capability of CMOS-compatible AlN fabrication platform to fulfil the requirements of MEMS Lidar. The micromirror aperture was set to 3 mm to avoid large micromirror deformations, although the preselected chip layout would have allowed for a larger aperture size. A tunable Lissajous scanning scheme meeting the specifications was demonstrated and shown to be accessible with low-voltage digital control methods.

Acknowledgments

The authors would like to thank all national funding authorities and the ECSEL Joint Undertaking, which funded the NewControl project under Grant Agreement No. 826653-2. The micromirror interfaces and electronics were developed under the NewControl project. The authors would like to thank the Finnish Government Organization Business Finland, which funded the 3D-LiDAR project under Grant Agreement No. 4345/31/2018VTT. The micromirror design and fabrication were done under the 3D-LiDAR project. We thank Murata Electronics Oy for micromirror packaging and mounting to ceramic carriers. The authors would like to express gratitude to their colleagues at the Micronova Research Centre for their assistance in the fabrication of the micromirrors, especially James Dekker and Panu Pekko, who played a main role

in the development of the PiezoMEMS process and Harri Pohjonen for the preparation of the masks for processing.

References

1. D. Wang, S. J. Koppal, and H. Xie, "A monolithic forward-view MEMS laser scanner with decoupled raster scanning and enlarged scanning angle for micro LIDAR applications," *J. Microelectromech. Syst.* **29**(5), 996–1001 (2020).
2. X. T. Nguyen et al., "A high-definition lidar system based on two-mirror deflection scanners," *IEEE Sens. J.* **18**(2), 559–568 (2018).
3. T. Pensala et al., "Wobbling mode ALN-Piezo-MEMS mirror enabling 360-degree field of view LIDAR for automotive applications," in *IEEE Int. Ultrason. Symp.*, pp. 1977–1980 (2019).
4. U. Hofmann et al., "Biaxial resonant 7-mm-MEMS mirror for automotive lidar application," in *Int. Conf. Opt. MEMS and Nanophotonics*, pp. 150–151 (2012).
5. A. Piot, J. Pribošek, and M. Moridi, "Dual-axis resonant scanning MEMS mirror with pulsed-laser-deposited barium-doped PZT," in *IEEE 34th Int. Conf. Micro Electro Mech. Syst.*, pp. 89–92 (2021).
6. D. Wang et al., "A low-voltage, low-current, digital-driven MEMS mirror for low-power lidar," *IEEE Sens. Lett.* **4**(8), 1–4 (2020).
7. N. Sarkar et al., "A large angle, low voltage, small footprint micromirror for eye tracking and near-eye display applications," in *Transducers—18th Int. Conf. Solid-State Sens., Actuators and Microsyst.*, pp. 855–858 (2015).
8. A. Yalcinkaya et al., "Two-axis electromagnetic microscanner for high resolution displays," *J. Microelectromech. Syst.* **15**(4), 786–794 (2006).
9. R. Ben-Mrad and D. Pasiliao, "A MEMS micromirror based head-up display system," in *Symp. Des., Test, Integr. and Packaging MEMS/MOEMS*, pp. 1–4 (2015).
10. S. Marauska et al., "Sputtered thin film piezoelectric aluminium nitride as a functional MEMS material and CMOS compatible process integration," *Procedia Eng.* **25**, 1341–1344 (2011).
11. M. Brennan et al., "On the jump-up and jump-down frequencies of the Duffing oscillator," *J. Sound Vib.* **318**(4-5), 1250–1261 (2008).
12. V. Kaajakari et al., "Nonlinear limits for single-crystal silicon microresonators," *J. Microelectromech. Syst.* **13**(5), 715–724 (2004).
13. K. S. Ruotsalainen and D. Morits, "Beam-steering MOEMS system based on a resonant piezoMEMS mirror and a phase-locked loop controller," *Proc. SPIE* **11697**, 116970I (2021).
14. V. Stenchly et al., "Viscous hot glass forming for optical wafer level packaging of micro mirrors," *Procedia Eng.* **47**, 64–67 (2012).
15. J. Park, S.-C. Byun, and B.-U. Lee, "Lens distortion correction using ideal image coordinates," *IEEE Trans. Consum. Electron.* **55**, 987–991 (2009).
16. F. Wu, H. Wei, and X. Wang, "Correction of image radial distortion based on division model," *Opt. Eng.* **56**(1), 013108 (2017).
17. S.-W. Eo et al., "ASIC design for real-time one-shot correction of optical aberrations and perspective distortion in microdisplay systems," *IEEE Access* **6**, 19478–19490 (2018).

Konsta Ruotsalainen received his BSc degree in embedded systems from the Applied University of Turku in 2008 and his MSc degree in micro- and nanoelectronics circuit design from Aalto University in 2016. He is a research scientist at the VTT Technical Research Centre of Finland Ltd. working on microelectronics interfaces, measurement techniques, and applications.

Dmitry Morits received his DSc (Tech) degree from Aalto University in 2014 for his works on the design composites for strong interaction with electromagnetic fields at optical and THz ranges. Later, he worked as a researcher at A*STAR, Singapore, in the field of nanophotonics. He is a research scientist at VTT Technical Research Centre of Finland. At VTT, he focuses on the design of MEMS devices for various applications.

Oili M. E. Ylivaara received her MSc (Eng) degree from Helsinki University of Technology in 2005. She is working at VTT Technical Research Centre of Finland Ltd. as a senior research scientist. Her experience is in front-end process development and integration.

Jukka Kyynäräinen received his MSc (Tech) and the DSc (Tech) degrees from Helsinki University of Technology, Espoo, Finland, in 1985 and 1990, respectively. From 1985 to 1997, he investigated superfluid ^{3}He at Helsinki University of Technology and polarized targets at CERN, Geneva, Switzerland. He joined the VTT MEMS sensors group in 1999 as a senior research scientist. His current research topics include micromechanical mirrors, pressure sensors, and inertial sensors.